

The dynamics and the merging scenario of the galaxy cluster ACT-CL J0102-4915, El Gordo

K. Y. Ng¹, W. A. Dawson², D. Wittman¹, J. Jee¹, J. Hughes³, F. Menanteau³, C. Sifón⁴
(temporary order)

¹*Department of Physics, University of California Davis, One Shields Avenue, Davis, CA 95616, USA*

²*Lawrence Livermore National Laboratory, P.O. Box 808, Livermore, CA 94551-0808, USA*

³*Department of Physics & Astronomy, Rutgers University, 136 Frelinghysen Rd., Piscataway, NJ 08854, USA*

⁴*Leiden Observatory, Leiden University, PO Box 9513, NL-2300 RA Leiden, Netherlands*

arXiv 666

ABSTRACT

Merging galaxy clusters with radio relics provide rare insights to the merger dynamics as the relics are created by the violent merger process. We demonstrate one of the first uses of the properties of the radio relic to reduce the uncertainties of the dynamical variables and 3D configurations of a cluster merger, ACT-CL J0102-4915, El Gordo. At a redshift of 0.87, El Gordo ($M_{200c} = 2.75 \times 10^{15} \pm_{1.5}^{7.4} M_{\odot}$) is one of the most massive clusters discovered in the early universe. The two subclusters of El Gordo has a mass ratio of around 2:1. The X-ray and weak-lensing data of El Gordo show an offset of X kpc between the intercluster gas and the dark matter (DM) at $\sim 4\sigma$ level. All these features of El Gordo make it part of a valuable class of dissociative mergers that can probe the self-interaction of dark matter. We employ a Monte Carlo simulation to investigate the three-dimensional (3D) configuration and dynamics of El Gordo. We give a summary of the inferred dynamical variables. By making use the polarization, velocity and position of the radio relic, we are able to confirm at $X\sigma$ that the subclusters of El Gordo are moving away from each other. We find that the 3D merger speed of El Gordo to be $\sim 3000 \text{ km s}^{-1}$, which is still consistent with the low line-of-sight velocity of $\sim 600 \text{ km s}^{-1}$ based on the inferred time-since-collision ($TSC = \text{Gyrs}$) and the projection angle ($\alpha = 41^{\circ} \pm$). We put our estimates of TSC and α into context by relating them to existing observations of El Gordo. Finally, we compare our simulation result of El Gordo to the simulation result of the Bullet Cluster, and show that El Gordo is a very promising candidate for giving tighter constraint than the Bullet Cluster on the self-interaction of dark matter. (200 words) (check against astro-ph word limit)

Key words: gravitational lensing – dark matter – cosmology: observations – X-rays: galaxies: clusters – galaxies: clusters: individual (ACT-CL J0102-4915) – galaxies: high redshift

1 INTRODUCTION

(NOT READY FOR PRIME TIME)

Mergers of dark-matter-dominated galaxy clusters probes properties of the cluster components like no other systems. Clusters of galaxies are made up of 80% of dark matter in mass content, with a smaller portion of inter-cluster gas ($\sim 15\%$ in mass content), and sparsely spaced galaxies ($\sim 2\%$ in mass content) (REF). During a merger of clusters, the subclusters are accelerated to high speeds of several thousand km s^{-1} . The offsets of different components of the subclusters dissociate show how various interactions

of the different components are at work. Observables such as offset between dark matter and the other components may suggest dark matter self-interaction (REF). (The following sentence does not actually fit in this paragraph and I have to put it somewhere else) difference of the galaxy colors in a merging cluster from relaxed cluster can also verify effects of environment on galaxy evolution.

Ever since the discovery of El Gordo in the Atacama Camera Telescope (ACT) survey (REF), there is an ongoing effort for collecting comprehensive data for El Gordo. The presence of the radio relic, in conjunction with a depression in the X-ray surface brightness shown in M11, strongly sug-

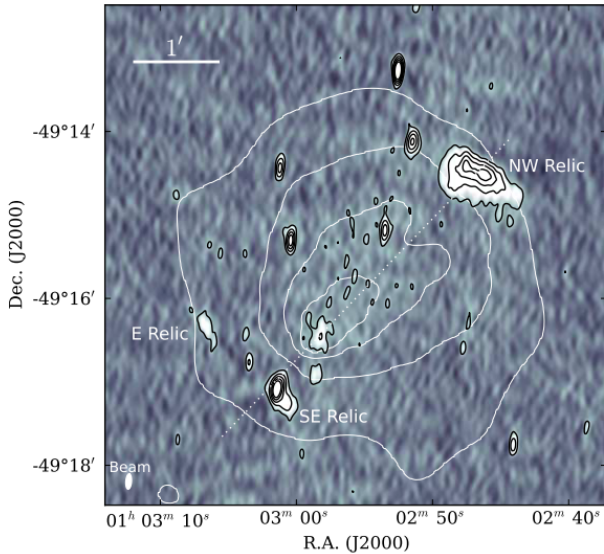


Figure 1. Configuration of El Gordo (to decide which figure to use, this one is from Lindner et al.)

gest that El Gordo is a post-collision system so we limit our discussion to inferring the time-since-collision.

From the spectroscopy and Dressler-Schechter test for the member galaxies in Sifón et al. (2013), El Gordo is confirmed to be a binary merger without significant substructures. This picture is further supported by the weak lensing analysis by Jee et al. (2013). The weak lensing analysis shows a mass ratio of $\sim 2:1$ between the two main subclusters, named according to their location as the northeast (NW) and southeast (SE) subclusters respectively. (See Figure 1). El Gordo has interesting intracluster medium morphology as shown in the X-ray. In the northwest, it shows a wake feature, i.e., depression in the X-ray emissivity, while in the southeast, it shows highest X-ray emissivity indicative of a cold gas core southeast of the wake. The cold gas core may have passed from the northwest to the southwest to have caused this morphology (Menanteau et al. 2011, hereafter M11). The extended mass distribution of El Gordo also makes it a good gravitational lens. Zitrin et al. (2013) have found multiple strong gravitationally lensed images around the center region of El Gordo. On the outer skirt of El Gordo, strong radio emission is detected in the NW and the SE respectively. These radio emission has steep spectral index gradient and are identified as radio relic created from a merger.

El Gordo is one of small sample of galaxy clusters (~ 50) that have been associated with a radio relic. (This paragraph needs a lot more organization) Even fewer of them have been studied in great details, making El Gordo a valuable candidate for further analysis. Furthermore, El Gordo satisfies the four criteria for being a dissociative merger which are proposed to be excellent probes of self-interacting dark matter (Dawson et al. 2012). (1) The subclusters of El Gordo has a small ratio of mass, i.e. $\sim 2:1$ (Jee et al. 2013, hereafter J13). (2) The merger axis, the line joining the two subclusters, coincides with the alignment of the double radio relic propagating outward at the periphery of the cluster (Menanteau et al. 2012, hereafter M12). This suggests a simple merger configuration with small impact variables. (3) The

X-ray luminosity peak is shown to be offset from the weak-lensing peak by X kpc at $X\sigma$ level (J13). (4) The observation of the double radio relic suggests that the angle between the merger axis and the plane of the sky has to be reasonably small (M11, Lindner et al. 2013), or else the relic may appear as a halo instead. (Skillman et al. 2013)

In this paper, we perform results of simulations for modeling the time evolution of the mergers. Determining the time-since-collision of mergers of similar clusters helps us reconstruct different stages of a cluster merger. Mergers of clusters proceed on the time-scale of millions of year, observations of each cluster only provides a snapshot of a particular type of merger. In order to understand the merger process observationally, we need to capture and identify different stages of similar dissociative mergers.

Another crucial piece of missing information is the 3D configuration, i.e. the projection angle α , which contributes the largest amount of uncertainties to the dynamical variables (Dawson 2013). With a large projection angle α , the radio emission may appear as a radio halo instead. (Skillman et al. 2013)

This work is particularly important since it is forbiddingly expensive to simulate clusters similar to El Gordo in high resolution. The probability for finding an analog of El Gordo in a cosmological simulation is as low as % (M11). A realistic cosmological simulation of El Gordo is thus computationally expensive. Under the hierarchical picture of structure formation in the Λ CDM model, there is a rare chance for massive clusters like El Gordo to have formed at a redshift of $z = 0.87$. Staged simulation would not be able to probe the angular dependence. Both weak lensing analysis and BLAH DATA of El Gordo (Jee et al. 2013) has revealed a relatively simple bimodal mass distribution. The lack of complex substructures makes modeling of El Gordo with only two subclusters possible.

In this paper, we adopt the following conventions: (1) we assume the standard Λ CDM cosmology with $\Omega_m = 0.3$, $\Omega_\Lambda = 0.7$. (2) All confidence intervals are quoted at the 68% level unless otherwise stated. (3) All credible intervals (a.k.a. Bayesian confidence intervals that also takes into account prior probability) are also quoted at the 68% level unless otherwise stated and are central credible intervals. (4) All quoted masses (M_{200c}) are based on mass contained within r_{200} where the mass density is 200 times the critical density of the universe (ρ_{crit}) at the redshift of $z = 0.87$.

2 METHOD – MONTE CARLO SIMULATION

For this analysis, we made use of the collisionless dark-matter-only Monte Carlo modeling code written by Dawson (2013), hereafter (D13). In the code, the time evolution of the head-on merger was computed based on an analytical model assuming that the only dominant force is the gravitational attraction from the masses of two truncated Navarro-Frenk-White (hereafter NFW) DM halos. Other major assumptions for modeling systems with this code include negligible impact parameter and no self-interaction of dark matter.

In the Monte Carlo simulation, many realizations of the collision is computed from the inputs of each realization, including the data (\vec{D}) and the model variable (α).

Table 1. Properties of the sampling PDFs of the Monte Carlo simulation

Data	Units	μ	σ	Ref
$M_{200c_{NW}}$	$10^{14} M_{\odot}$			J13
c_{NW}	/			J13
$M_{200c_{SE}}$	$10^{14} M_{\odot}$			J13
c_{SE}	/			J13
z_{NW}	/	0.86901	0.00017 ^b	M11, Sifón 2013
z_{SE}	/	0.87175	0.00019 ^b	M11, Sifón 2013
d_{proj}	Mpc			J13

^aThis σ corresponds to the 68% central Bayesian credible interval computed from the posterior probability of our MCMC analysis.

^bThis σ corresponds to the biweight scale.

^cWe use the full PDFs as the inputs of our simulation so different ways of denoting the uncertainties do not affect the simulation.

In particular, the standard required data, which were in the form of samples of the probability density functions (PDFs), included the masses ($M_{200_{NW}}, M_{200_{SE}}$) the redshifts (z_{NW}, z_{SE}) and the projected separation of the two subclusters (d_{proj}). In each realization, we randomly drew samples of the PDFs. These inputs are then used for computing the output variables ($\vec{\theta}'$) by making use of conservation of energy to describe their collision due to the mutual gravitational attraction. (See Table 1 for quantitative descriptions of the sample PDFs and we outline how those PDFs are obtained in the following subsections.) To ensure convergence of the output PDFs, in total, 2 million (to be confirmed) realizations were computed. The results, however, are consistent up to a fraction of a percent just from 20 000 runs (D13).

We note that the Monte Carlo simulation is described from a Bayesian point of view but the analysis differs from conventional Bayesian inference. The Bayes chain rule underlies the simulation can be written as:

$$P(\vec{\theta}|\vec{D}) \propto P(\vec{D}|\vec{\theta})P(\vec{\theta}) \quad (1)$$

where the likelihood is defined to be the PDF of \vec{D} given $\vec{\theta}$, i.e. the input variables, not statistical parameters, and the priors are defined to be the probabilities due to prior knowledge of the estimated values of $\vec{\theta}$. The output variables $\vec{\theta}'$, on the other hand, were computed according to the conservation of energy, which is represented by a suitable functional form f below. For example, the calculation of the output variables of the j -th realization can be denoted as:

$$(\vec{\theta}')^{(j)} = f(\vec{\theta}^{(j)}, \vec{D}) \quad (2)$$

and computed over all j realizations. Finally, we took the physical constraints on $\vec{\theta}$ and $\vec{\theta}'$ into account by examining the resulting physical variables against the physical limits and excluding realizations that would produce impossible values. We refer to this process of excluding realizations as “applying prior probability”.

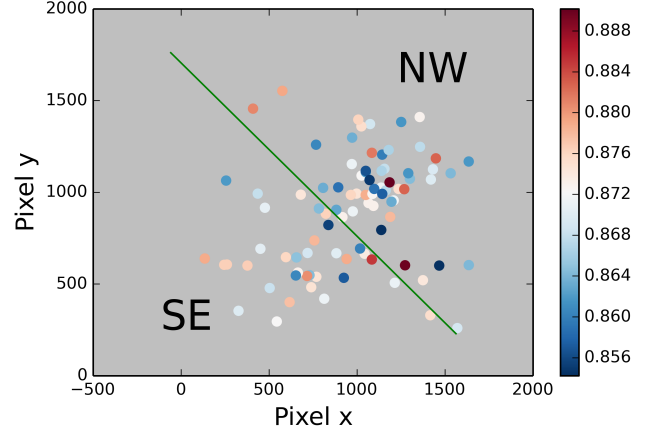


Figure 2. The division of the member galaxies among the two subclusters of El Gordo by a spatial cut (green line) that is approximately perpendicular to the 2D merger axis (M11). The color bar shows the color mapping of the spectroscopic redshift of the member galaxies. The spatial cut is done after mapping the world coordinates to pixel coordinates to avoid anamorphic distortion. (changed background to gray since Nick said the white background makes the dots hard to see)

2.1 Inputs of the Monte Carlo simulation

2.1.1 Membership selection and redshift estimation of subclusters

We used a 2D spatial cut to determine members of the two subclusters, then bootstrapped the biweight locations of the redshifts of the respective members in order to obtain the PDFs of the redshifts of each subcluster. We made use of the spectroscopic data obtained from the Very Large Telescope (VLT) and Gemini South as described in M11 and Sifón et al. (2013). The overall membership of the galaxies of El Gordo was determined using a shifting gapper method after applying a rest frame cut of 4000 km s^{-1} . This method gives a total count of 89 galaxy members of El Gordo. From the 2D spatial cut of the confirmed members, we determined that there are 54 members in the NW subclusters and 35 members in the SE subclusters (See Figure 2). The spectroscopic redshift of the clusters were determined to be $z_{NW} = 0.86901 \pm 0.00017$ and $z_{SE} = 0.87175 \pm 0.00019$, where the quoted numbers represent the biweight location and biweight scale respectively (Beers et al. 1990). The biweight location estimators are less susceptible to outliers than the mean and standard deviations.

2.1.2 Weak lensing mass estimation

We obtained the PDFs of the masses of the subclusters by doing a Monte Carlo Markov Chain (MCMC) analysis of the reduced shear from the weakly lensed background galaxies similar to Dawson et al. (2012). We computed the reduced shear signal generated by two NFW halos according to Umetsu (2010) (See Appendix A for details of implementation and output diagnostics). At each step we followed the procedure of a Metropolis algorithm. The transition kernel was set to be the log likelihood of fit of the model shear to the reduced shear of the data (A1). In total, eight MCMC

chains were used. After every 5000 MCMC steps for all the chains, we computed the R coefficient (Gelman & Rubin 1992) to check for convergence. We performed more MCMC steps as long as convergence was not achieved. After convergence was achieved, we removed the burn-in portions of the MCMC chains and used the resulting MCMC chains as samples of the PDFs of the masses.

We used a catalog of reduced and bias-corrected background galaxy shapes from Hubble Space Telescope PROP 12755 similar to J13. (! Jee et al. 2013 actually used additional data) On the other hand, we fixed the position of the centers of the NFW halos to be the luminosity peaks of the respective galaxy populations of the two subclusters, which are at R.A. = 01:02:51.68, Decl. = -49:15:04.40 and R.A. = 01:02:38.38, Decl. = -49:16:37.64 for the NW and SE subclusters respectively (J13). (! Lori and Nick actually asked why we do not free the centroids like Jee 13) The agreement between our analysis and (J13) to within the 68% credible interval serves as a sanity check on the estimated masses.

2.1.3 Estimation of projected separation (d_{proj})

To be consistent with our MCMC mass inference, our Monte Carlo simulation takes the projected separation of the NFW halos to be those of the two aforementioned luminosity peaks.

2.2 Outputs of the Monte Carlo simulation

We outline the outputs of the simulation here to facilitate the discussion of the design of the priors used in the simulation. The simulation provides PDF estimates for many of the output variables. Variables of the most interest include the time dependence and α , which is defined to be the projection angle between the plane of the sky and the merger axis. Other output variables are dependent on α and the time dependence. Specifically, the simulation denotes the time dependence by providing several characteristic timescales, including the time elapsed between the collision and when the subclusters first reach apoapsis (T) and the time-since-collision.

The two versions of the time-since-collision variables TSC_0 and TSC_1 denotes different possible merger scenarios. 1) We call the scenario for which the subclusters are moving apart after collision to be “outgoing” and it corresponds to the smaller TSC_0 value, and 2) we call the alternative scenario “incoming” for which the subclusters are approaching each other after turning around from the apoapsis for the first time and it corresponds to TSC_1 . We describe how we use to break the degeneracies of the two scenarios in section 2.4.

The simulation also output estimates of variables that characterize the dynamics of the merger. The 3D velocities, both at the time of the collision ($v_{3D}(t_{col})$) and at the time of observation ($v_{3D}(t_{obs})$) are provided. The maximum 3D separation (d_{max}), which is defined to be the distance between the position of collision to the apoapsis, is also part of the outputs. (See the lower half of Table 2 for all the outputs).

2.3 Design and application of priors

The strength of the Monte Carlo simulation by D13 is its ability to detect and rule out extreme input values that would result in unphysical realizations via the application of prior probability. Our default Monte Carlo priors are described in D13 and in Appendix B. We also examine the effects of applying two priors derived based on the position and the integrated polarization fraction of the radio relic of El Gordo respectively. (* I actually removed the position prior section from the paper since the position prior does not provide tight constraint on the parameters).

(Not sure if the following fits best here but it is definitely an intro to the priors) El Gordo shows radio relics on the periphery of both subclusters (M11). The radio relic of El Gordo was first mentioned in the Sydney University Molonglo Sky Survey (SUMSS) data in low resolution at 843 MHz (Mauch et al. 2003) as shown in M11. The higher resolution radio observation conducted by Lindner et al. (2013) at 610 MHz and 2.1 GHz confirms that the identity of the radio relic after removing effects of radio point sources. Three main sources of radio relic were identified, including the NW, SE and the E relic. The NW radio relic possesses the most extended geometry among all the identified relic source. We do not refer to the SE nor the E radio relic in our calculation since we do not have an estimation of the shock speed of the SE relic nor the E relic from Lindner et al. (2013) for comparison.

2.3.1 Monte Carlo priors based on the polarization fraction of the radio relic

In the presence of a uniform magnetic field, the observed polarization fraction of the synchrotron emission of the electrons depends on the viewing angle with respect to the alignment of the magnetic field. Synchrotron emission from electrons inside unorganized magnetic field are randomly polarized. The high reported integrated polarization fraction from Lindner et al. (2013) can be explained by a highly aligned magnetic field, created by the compressed intracluster medium during a merger (Ensslin et al. 1998, van Weeren et al. 2010, Feretti et al. 2012). This picture is consistent with a high polarization fraction perpendicular to this magnetic field along the relic.

The major assumption behind the design of our filter is that the integrated polarization fraction is a monotonically decreasing function of α . This assumption is inspired by the class of models given by Ensslin et al. (1998), which, despite various inputs for spectral indices and magnetic field strength, each predicts a monotonically decreasing integrated polarization fraction as a function of α . In particular, we refer to a model from Ensslin et al. (1998) that would give the most conservative estimate on the upper bound of α . This model predicts a maximum integrated polarization fraction of $\sim 75\%$ when $\alpha = 0$. From this model, the observed integrated polarization fraction of 33% corresponds to $\mu_\alpha = 39^\circ$. This polarization fraction of $\sim 75\%$ predicted by (Ensslin et al. 1998) is consistent with the upper bound of relic polarization fraction in cosmological simulations (Skillman et al. 2013). No other model of the magnetic field should predict a higher polarization fraction, thus it is

Table 2. Table of the output PDF properties of the model variables and output variables from Monte Carlo simulation

		Default priors		Default + position priors			
Variables	Units	Location	68% CI [†]	95% CI	Location	68% CI	95% CI
α	(degree)						
TSC_0	Gyr						
TSC_1	Gyr						
T	Gyr						
d_{max}	Mpc						
$v_{3D}(t_{obs})$	km s ⁻¹						
$v_{3D}(t_{col})$	km s ⁻¹						
d_{max}	Mpc						
d_{3D}	Mpc						

† CI stands for credible interval

highly unlikely that we see 33% integrated polarization at $\alpha > 39^\circ$.

We cannot rule out $\alpha \leq 39^\circ$ as a result of possible variations in the magnetic field. Ensslin et al. (1998) assumes an isotropic distribution of electrons in an isotropic magnetic field. Cosmological simulations of radio relics from Skillman et al. (2013) show varying polarization fraction across and along the relic assuming $\alpha = 0$, resulting in a lower integrated polarization fraction. For example, it is possible to see a edge-on radio relic ($\alpha = 0$) with integrated polarization fraction of 33%. To summarize, the prior derived from polarization information takes the form of:

$$P(\alpha) = \begin{cases} \text{const.} > 0 & \text{for } \alpha < 39^\circ \\ 0 & \text{otherwise} \end{cases} \quad (3)$$

(I removed the figure showing the prior and replaced it with the above equations since the equation is more compact.)

Observation also introduces uncertainties that we have to take into account. Skillman et al. (2013) shows that after convolving the simulated polarization signal with a Gaussian kernel of $4'$ to match the observed resolution, the polarization fraction drops to between 30% to 65% even when $\alpha = 0$. Other uncertainties come from the fact that the inferred spectral indices differ between the two observed frequencies and vary between the three identified relic sources (Lindner et al. 2013). We examine the effects of changing the cutoff value of this prior to ensure the uncertainties do not introduce significant bias in the estimated output variables and we present the results in Appendix B.

2.4 Extension to the Monte Carlo simulation - Determining merger scenario with radio relic position

We give constraints on the likelihood of the outgoing and incoming merger scenarios by comparing the observed and the simulated position of the NW radio relic. This method depends the estimate of the time evolution of the relic velocity, which gives the upper and lower bounds on the possible position of the relic for each scenario. The uncertainty of velocity stem depends on a number of physical quantities, including the local gravitational potential, matter density, temperature, pressure among others (Ensslin et al. 1998, Shu .F., more citations?). The exact time evolution of the

shock velocity requires detailed numerical simulation similar to Springel & Farrar (2007), Vazza et al. (2012), Kang et al. (2007), etc. We considered different possibilities of the time evolution of the shock velocity since numerical simulation of the shock of El Gordo is not available at the time of writing of this paper. We drew physical insight from the simulations of the merger shock of the staged numerical simulation of the Bullet cluster from Springel & Farrar (2007) and the cosmological simulation from Paul et al. (2011). Right after the collision of the subclusters, Springel & Farrar (2007) shows that the shock speed is comparable to the merger speed of the two subclusters; the shock speed dropped only by $\sim 14\%$ in the 300 Myr period while the speed of the main subcluster in the simulation dropped by $\sim 65\%$ in the center of mass frame. On the other hand, Paul et al. (2011) showed that the shock speed was ~ 1.5 times the relative collisional speed of the subcluster shortly after the collision and the shock speed decreases only slightly as it propagates away from the center of mass.

We approximated the upper and lower bounds of the NW relic speed with the simulated speeds of the NW subcluster. We simplified the calculation by working in the center of mass frame where the shock speed is expected to drop slightly with time. The projected separation of the shock is approximated as:

$$s_{proj} = \langle v_{relic} \rangle (\hat{t}_{obs} - \hat{t}_{col}) \cos(\hat{\alpha}) \quad (4)$$

where the quantities with hats on the right hand side of the equations were inferred from the simulation, and s_{proj} is the estimated projected separation and we estimated the upper and lower bounds of the time-averaged velocity $\langle v_{relic} \rangle$ of the shock between the collision of the subclusters and the observed time as:

$$\langle v_{relic} \rangle = \beta v_{3D,1}(t_{col}) \quad (5)$$

where $0.8 \leq \beta \leq 1.2$ is a factor that we introduce to represent the uncertainty of the speed of the relic and $v_{3D,1}(t_{col})$ refers to the collisional velocity of the NW relic in the center-of-mass frame. The upper bound can be approximated as the collisional speed of the NW subclusters due to how the shock is powered by the collision. After the collision, it is unlikely that there would be significant energy injected into the shock to speed up the shock such that the shock travels much faster than the collision speed of the subcluster. While the shock does not experience gravitational decelera-

tion as a pressure wave, some dissipative processes may have slowed down the shock wave slightly as it propagated. By making use of a range of β values, we examine the how the rate of slow down would give a different lower bound of the projected separation of the relic.

3 RESULTS

*(Not ready for prime time) We estimated the relative merger speed of the two subclusters to be 3400 km s^{-1} at the time of collision. There have been several estimates of the relative merger speed based on different physics. For example, Lindner et al. (2013) inferred the upper bound of the relative collisional velocity from the Mach number of the NW radio relic, giving an upper bound estimate of $4300 \pm_{500}^{800} \text{ km s}^{-1}$. This speed is compatible with our simulated collisional speed within the uncertainty. However, we note that the conversion of the frame of reference is non-trivial since the speed is measured with respect to the turbulent intracluster gas as a Mach number. Based on the observed peculiar velocity difference between the galaxies of the two subclusters, $v_{3D}(t_{col}) \approx v_{pec}(t_{obs})/\sin(\alpha)$, M11 gave two estimates:

$$v_{3D}(t_{col}) = 596/\sin(\alpha) \text{ km s}^{-1} = \begin{cases} 2300 \text{ km s}^{-1}, & \alpha = 15^\circ \\ 1200 \text{ km s}^{-1}, & \alpha = 30^\circ \end{cases} \quad (6)$$

If we use our estimate of $\alpha = 41.7^\circ$ in (6), we obtain an estimate of $v_{3D}(t_{obs}) \approx 895 \text{ km s}^{-1}$ instead. This is consistent with our simulation, the two subclusters are estimated to slow down to a 3D relative velocity of only $v_{3D}(t_{col}) \sim 800 \text{ km s}^{-1}$.

3.1 Time-since-collision

The simulation gives two plausible estimates for the time-since-collision, with $TSC_0 = 0.6 \text{ Gyr}$ and $TSC_1 = 1.0 \text{ Gyr}$ (TO BE CONFIRMED). Based on section 2.4, we present estimates for the position of the NW radio relic based on the two PDFs of inferred TSC as shown in Fig. 3, using the default priors. We plotted the PDF of the simulated positions of the relic for the outgoing scenario (blue) and the incoming scenario (green) against the observed position of the relic (light red), with the width of the relic accounting for the reported physical width (23 kpc) of the relic along the merger axis (Lindner et al. 2013). When we assume $\langle v_{relic} \rangle / v_{3D,1}(t_{col}) = 1.2$ (uppermost panel of Figure 3), which is approximately the upper limit of how fast the shock can travel, the outgoing scenario is more favored. As we examine a decreased ratio of $\langle v_{relic} \rangle / v_{3D,1}(t_{col})$, we probe how much the shock could have slowed down and still be consistent with the outgoing scenario. The third and forth row of Fig. 3 show that if $\langle v_{relic} \rangle \lesssim 0.95$, the incoming scenario would be favored instead. For those speeds, the outgoing scenario could be incompatible as the projected relic location could be smaller than the observed NW subcluster indicated by the yellow line. After taking into account the polarization information (Fig. B1), the incoming scenario is even more favored but a definite conclusion about the correct scenario would require better knowledge of the time evolution of the shock velocities.

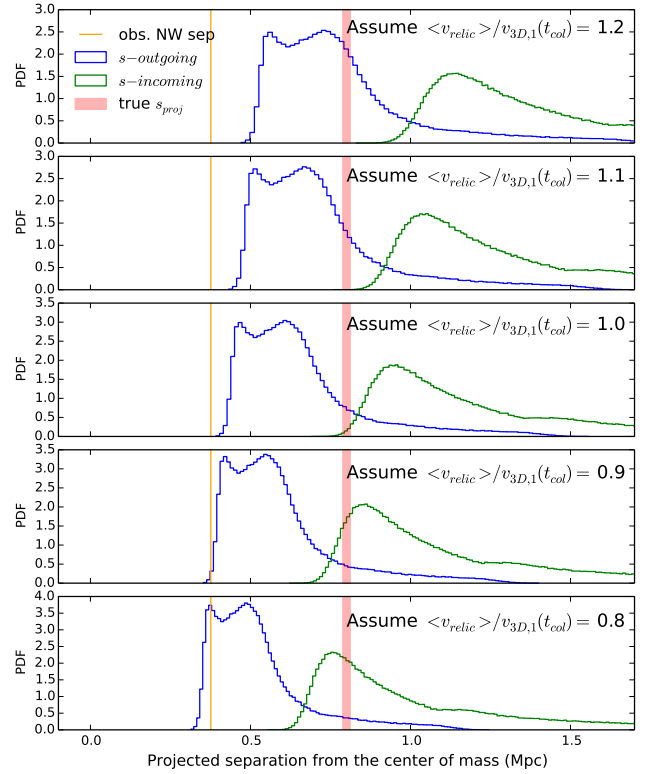


Figure 3. Comparison of the observed position of the relic (red) with the predicted position from the two simulated merger scenarios (blue for outgoing and green for the incoming scenario). The outgoing scenario is more favored than the incoming scenario since the shock speed is unlikely to travel at much less than $0.6 v_{3D,1}(t_{col})$ for a significant period of time. Default priors were used for this figure. Alternate version of this figure with the polarization prior applied can be found in Appendix B.

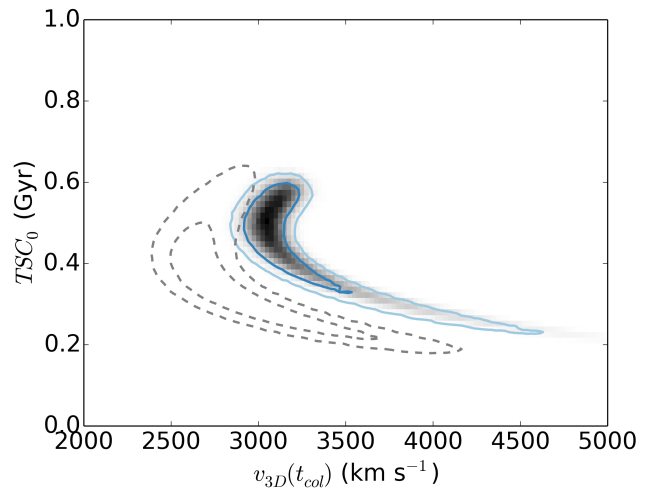


Figure 4. The marginalized outgoing time-since-collision (TSC_0) vs 3D velocities (v_{3D}) of El Gordo and the Bullet Cluster. (to add descriptions of the different filters used)

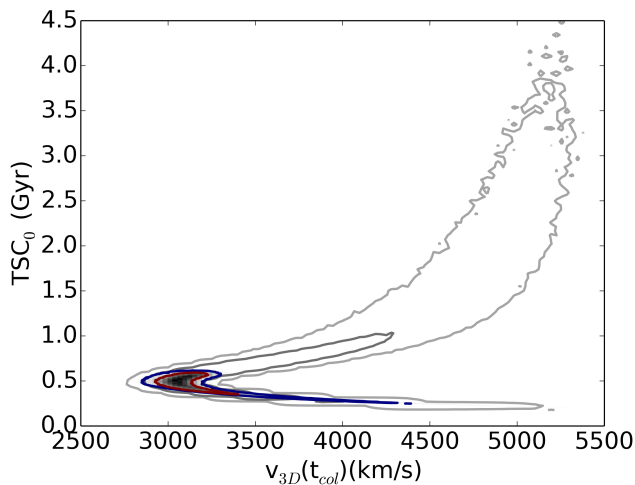


Figure 5. The marginalized output PDF of the outgoing time-since-collision (TSC_0) vs. the 3D velocity at the time of collision for El Gordo. (to add more description about contours)

3.2 Effects of applied prior on output variables

We perform tests of how sensitive our parameters are to the design of our prior filters and found that shifting of the cutoff values by 5% would only affect the inferred values by X%.

3.3 Three-dimensional (3D) configuration of El Gordo

The Monte Carlo simulation estimates that the projection angle to be 41.7° , with the CI = 22.7° , 61.14° . Our estimate is consistent with the estimate of $\alpha > 7.8^\circ$ from Lindner et al. (2013). Many previous studies (CITATIONS) have suggested that α should be small for the detection of double radio relics.

- explains that there hasn't been quantitative constraints on the angle for which double radio relic can be observed, even though that many studies have suggested that the detection of radio relic should imply that α should be small. From this simulation we have shown that it is possible to detect the double radio relics with α being as big as 61.14° .

- Lindner et al. provided constraint of $\alpha > 7.8^\circ$ based on the dynamics.

- James' paper did mention how the mass estimation depends on α , with the estimated mass being a lot smaller if $\alpha \geq 65^\circ$. However, since we did use the larger mass estimate as the input of this simulation, we can only say that the inferred α is consistent with the mass estimation.

- discussion of the different scenarios mention in M11: 1) we are viewing after core passage, but before first turn around, and the merger speed is low"

- 2) the merger speed is high, but we are viewing after the first turn around as the two components come together for a second core passage

- discuss the inclination angle estimate from M11

- Dave: explain where the limits of the projection angle comes from. what observational evidence contradicts the low velocity scenario the most

With this new piece of evidence, we find that the absence of an X-ray shock feature from El Gordo, may not be due to the merger speed being low, as suggested by (J13). In particular, taking into account that the estimated projection angle of $\sim 41.7^\circ$, we estimate the projected relative velocity to be 597 km s^{-1} , which is consistent with the estimated line-of-sight velocity differences of $586 \pm 96 \text{ km s}^{-1}$ in M11.

Furthermore, the study from Lindner et al. (2013) Lindner et al. has come up with an estimation of the shock velocity of the radio relic of El Gordo as $\sim 4000 \text{ km s}^{-1}$. While this shock velocity is not the same as the merger velocity, they should be of similar magnitude. Indeed our simulation found that a merger velocity of 4000 km s^{-1} is within the 95% credible interval.

4 DISCUSSION

4.1 Our finding in the context of other studies of El Gordo

Compare to Lindner et al. (2013). Compare to Donnert (2013) for their best fit scenario.

4.2 Comparison to other merger clusters of galaxies

Talks about how El Gordo is more massive and collided at higher speed than both the Bullet and the Musketball, so El Gordo is probably a better probe of SIDM properties.

With this new piece of evidence, we find that the absence of an X-ray shock feature from El Gordo, may not be due to the merger speed being low, as suggested by J13. In particular, taking into account that the estimated projection angle of $\sim 41.7^\circ$, we estimate the projected relative velocity to be 597 km s^{-1} , which is consistent with the estimated line-of-sight velocity differences of $586 \pm 96 \text{ km s}^{-1}$ in M11.

Furthermore, the study from Lindner et al. (2013) Lindner et al. has come up with an estimation of the shock velocity of the radio relic of El Gordo as $\sim 4000 \text{ km s}^{-1}$. While this shock velocity is not the same as the merger velocity, they should be of similar magnitude. Indeed our simulation found that a merger velocity of 4000 km s^{-1} is within the 95% credible interval.

4.3 Possible improvements for the radio relic prior

needs better simulation to understand the physical properties of radio relic.

4.4 Limitations of our model and future work

Impact parameter of El Gordo may not be negligible. Simulations from Ricker & Sarazin (2001) showed that cool-core is not disrupted when the impact parameters of mergers are of the order of $\sim 500 \text{ kpc}$.

5 SUMMARY & CONCLUSION

This paper presents one of the first examples of using the observed radio relic emission to constrain cluster merger properties. While we have demonstrated how to use the physical properties of the radio relic emission to constrain merger dynamics and configurations, many improvements can still be made as more studies of radio relic are being done from both cosmological simulations and observations.

Currently, there are only a few studies of radio relic available for a range of viewing angles ((**alias?**), one of Bruggen's paper). As more cosmological simulations inform us if the relic is observable at certain viewing angles will help us come up with better Monte Carlo filters.

6 ACKNOWLEDGEMENTS

We thank Franco Vazza and Marcus Brüggen for sharing their knowledge on the simulated properties of radio relic. We extend our gratitude to Reinout Van Weeren for first proposing the use of radio relic as prior. We appreciate the comments from Maruša Bradač about using the position of the relic to break degeneracy of the merger scenario.

REFERENCES

- Beers T. C., Flynn K., Gebhardt K., 1990, *AJ*, 100, 32, doi:10.1086/115487
- Dawson W. A., 2013, *ApJ*, 772, 131, 1210.0014, doi:10.1088/0004-637X/772/2/131
- Dawson W. A. et al., 2012, *ApJ*, 747, L42, 1110.4391, doi:10.1088/2041-8205/747/2/L42
- Donnert J. M. F., 2013, 14, 1, 1311.7066
- Ensslin T. A., Biermann P. L., Klein U., Kohle S., 1998, *A&A*, 332, 395, 9712293
- Feretti L., Giovannini G., Govoni F., Murgia M., 2012, *aapr*, 20, 58, 1205.1919
- Gelman A., Rubin D. B., 1992, *Stat. Sci.*, 7, 457
- Jee M. J., Hughes J. P., Menanteau F., Sifon C., Mandelbaum R., Barrientos L. F., Infante L., Ng K. Y., 2013, 1309.5097
- Kang H., Ryu D., Cen R., Ostriker J. P., 2007, *ApJ*, 669, 729, doi:10.1086/521717
- Lindner R. R. et al., 2013, p. 22, 1310.6786
- Mauch T., Murphy T., Buttery H. J., Curran J., Hunstead R. W., Piestrzynski B., Robertson J. G., Sadler E. M., 2003, *MNRAS*, 342, 1117, doi:10.1046/j.1365-8711.2003.06605.x
- Menanteau F. et al., 2012, *ApJ*, 748, 7, 1109.0953, doi:10.1088/0004-637X/748/1/7
- Paul S., Iapichino L., Miniati F., Bagchi J., Mannheim K., 2011, *ApJ*, 726, 17, doi:10.1088/0004-637X/726/1/17
- Roberts G. O., Gelman A., Gilks W. R., 1997, *Ann. Appl. Probab.*, 7, 110
- Sifón C. et al., 2013, *ApJ*, 772, 25, 1201.0991, doi:10.1088/0004-637X/772/1/25
- Skillman S. W., Xu H., Hallman E. J., O'Shea B. W., Burns J. O., Li H., Collins D. C., Norman M. L., 2013, *ApJ*, 765, 21, doi:10.1088/0004-637X/765/1/21
- Springel V., Farrar G. R., 2007, *MNRAS*, 380, 911, doi:10.1111/j.1365-2966.2007.12159.x

Umetsu K., 2010, p. 30, 1002.3952, doi:10.3254/978-1-60750-819-9-269

van Weeren R. J., Röttgering H. J. a., Brüggen M., Hoeft M., 2010, *Science*, 330, 347, doi:10.1126/science.1194293

Vazza F., Brüggen M., van Weeren R., Bonafede A., Dolag K., Brunetti G., 2012, *MNRAS*, 421, 1868, 1111.1720, doi:10.1111/j.1365-2966.2011.20160.x

APPENDIX A: DETAILS AND OUTPUT DIAGNOSTICS FOR THE MCMC MASS INFERENCE

The reduced shear generated by each NFW halo is determined by its mass (m_{200c}) and the position of its center (\vec{s}).

We consider the joint posterior as the fit to the ellipticity data:

$$\log(P(m_1, m_2 | \vec{e})) \propto - \left[\frac{(\hat{e}_1(m_1, m_2) - e_1)^2}{\sigma_{e_1}^2 + \sigma_{SN}^2} + \frac{(\hat{e}_2(m_1, m_2) - e_2)^2}{\sigma_{e_2}^2 + \sigma_{SN}^2} \right] \quad (A1)$$

where we have fixed the centers of the halos so \vec{s}_1 and \vec{s}_2 so \vec{s}_1 and \vec{s}_2 are left out of the joint posterior.

Gaussian shape noise of the background galaxies are represented by $\sigma_{SN} = 0.25$ (to be checked) represents Gaussian shape noise of the background galaxies; The reduced shear due to the NFW halos can be decomposed into two components, \hat{e}_1 and \hat{e}_2

We apply a uniform prior and only drew starting mass values between $10^{13} M_\odot$ and $10^{15} M_\odot$ for our MCMC chains, as informed by previous published mass estimates. (M11, J13, Zitrin et al. 2013). Each of the subsequent MCMC step then draws a random pairs of mass value with the values of previous step as the means of the distributions. (THERE SHOULD BE A TRACE PLOT HERE REPORTING THE ACCEPTANCE RATE.) We control the variance such that an optimal acceptance rate of the Metropolis algorithm of ~ 0.234 (Roberts et al. 1997) is achieved .

APPENDIX B: PLOTS OF OUTPUTS OF THE MONTE CARLO SIMULATION

(make sure that there are charts showing the TSC and alpha and velocities before this figure or else it may be confusing to readers)

This paper has been typeset from a \LaTeX file prepared by the author.

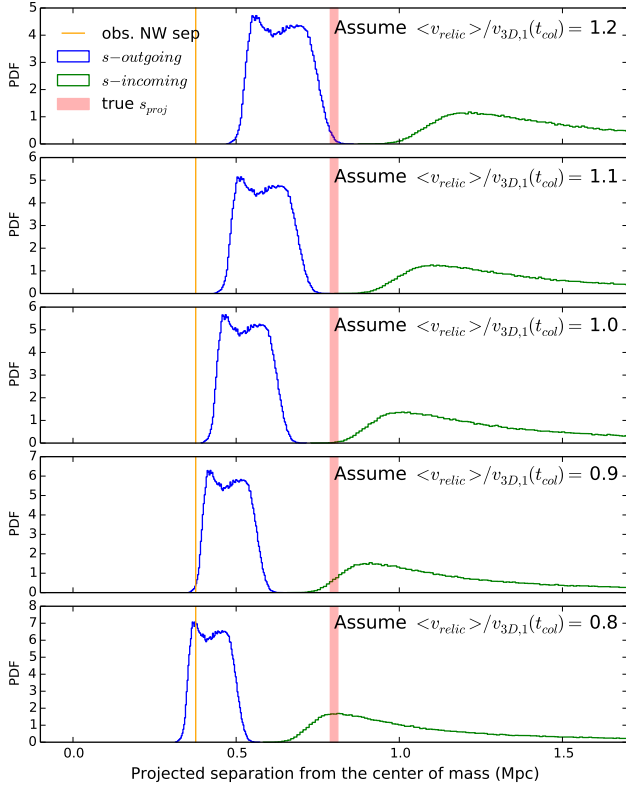


Figure B1. Comparison of the observed position of the relic with the predicted position from the two simulated merger scenarios, with polarization prior applied to the PDFs.